ARTICLE

Check for updates

Superconductivity induced by gate-driven hydrogen intercalation in the charge-density-wave compound 1T-TiSe$_2$

Erik Piatti [1✉], Giacomo Prando [2], Martina Meinero[3,4], Cesare Tresca [5,6], Marina Putti[3,4], Stefano Roddaro [7], Gianrico Lamura[3], Toni Shiroka[8,9], Pietro Carretta[2], Gianni Profeta[5,6], Dario Daghero [1] & Renato S. Gonnelli [1✉]

Hydrogen (H) plays a key role in the near-to-room temperature superconductivity of hydrides at megabar pressures. This suggests that H doping could have similar effects on the electronic and phononic spectra of materials at ambient pressure as well. Here, we demonstrate the non-volatile control of the electronic ground state of titanium diselenide (1T-TiSe$_2$) via ionic liquid gating-driven H intercalation. This protonation induces a superconducting phase, observed together with a charge-density wave through most of the phase diagram, with nearly doping-independent transition temperatures. The H-induced superconducting phase is possibly gapless-like and multi-band in nature, in contrast with those induced in TiSe$_2$ via copper, lithium, and electrostatic doping. This unique behavior is supported by ab initio calculations showing that high concentrations of H dopants induce a full reconstruction of the bandstructure, although with little coupling between electrons and high-frequency H phonons. Our findings provide a promising approach for engineering the ground state of transition metal dichalcogenides and other layered materials via gate-controlled protonation.

[1] Department of Applied Science and Technology, Politecnico di Torino, I-10129 Torino, Italy. [2] Dipartimento di Fisica, Università degli Studi di Pavia, I-27100 Pavia, Italy. [3] Consiglio Nazionale delle Ricerche-SPIN, I-16152 Genova, Italy. [4] Department of Physics, Università di Genova, I-16146 Genova, Italy. [5] Department of Physical and Chemical Sciences, Università degli Studi dell'Aquila, I-67100 L'Aquila, Italy. [6] SPIN-CNR, Università degli Studi dell'Aquila, I-67100 L'Aquila, Italy. [7] Istituto Nanoscienze-CNR, NEST and Scuola Normale Superiore, I-56127 Pisa, Italy. [8] Laboratory for Muon-Spin Spectroscopy, Paul Scherrer Institut, CH-5232 Villigen PSI, Switzerland. [9] Laboratorium für Festkörperphysik, ETH Zürich, CH-8093 Zürich, Switzerland. ✉email: erik.piatti@polito.it; renato.gonnelli@polito.it

The recent observation of near-to-room-temperature superconductivity in hydrides under high pressure[1,2] has demonstrated that a superconducting (SC) state with high critical temperature does not necessarily require an unconventional electron–electron coupling mechanism. The key requirements here are high phonon frequencies, such as those associated to the hydrogen (H) vibration modes, a strong coupling of these modes to the electronic states at the Fermi level, and a non-conventional structural environment (in the specific case, stabilized by pressure) that favors such a coupling. A still-open question is whether these same ingredients can be used to design new SC materials at ambient pressure—with properties of interest for applications even though at lower temperatures—or a different paradigm must be considered when designing H-rich superconductors at low pressures. This point is especially relevant in light of the recently-claimed attainment of room-temperature superconductivity in lutetium hydride at relatively low pressures[3].

One of the routes to create H-rich materials is ionic liquid gating-induced protonation. As this technique makes it possible to insert H atoms in crystallographic positions unattainable by a conventional synthesis approach, it has found notable applications in oxides[4–9] and demonstrated a great potential in layered materials as well[10,11]. Among the latter, transition metal dichalcogenides (TMDs) are particularly interesting because, despite their structural simplicity, they exhibit a variety of quantum phases[12,13]—charge-density wave (CDW), ferromagnetism, Mott insulating state, etc.—that may be tuned by protonation. In some cases, TMDs display a topological order, hence, once made SC, they may host Majorana fermions[14,15]. TMDs are also easy to handle and can be used to fabricate electronic devices[16–18], even printed ones[19,20]. Hence, by tailoring their physical properties, one can realize good and affordable prototypes for various quantum-technology applications, SC electronics, or quantum computing[21]. In this context, the archetypal TMD compound titanium diselenide ($1T$-TiSe$_2$) is an ideal candidate to benchmark the ionic-gating-induced protonation technique, since it exhibits strong electron–electron correlations and a variety of intriguing quantum phases[16], akin to those found in other layered materials such as iron-based compounds[22,23], cuprates[24], and heavy-fermion systems[25]. Furthermore, the electronic ground state of $1T$-TiSe$_2$ is readily tunable by a variety of different methods, including chemical intercalation[26–28], applied pressure[29], and electrostatic gating[30,31].

In this work, we show that protonation of TMDs induced by ionic liquid gating is a powerful and unique doping technique to control their electronic ground state. In particular, we demonstrate that it allows a robust and non-volatile control over CDW and SC in $1T$-TiSe$_2$. These two quantum phases dominate the phase diagram of $1T$-TiSe$_2$ and are found to coexist across all the investigated H doping levels. Fully protonated H$_x$TiSe$_2$ samples exhibit an impressive doping level (x ≈ 2), with negligible structural alterations, vestigial CDW signatures, and robust bulk superconductivity with possible multi-band and gapless features revealed by different experimental techniques. Our calculations indicate that these peculiarities of protonated TiSe$_2$ are caused by the unique capability of H atoms to act not only as pure electron donors since, at sufficiently large H concentrations, their doping becomes band-selective and fills the Ti-d_{z^2} bands, allowing the band structure of $1T$-TiSe$_2$ to mimic that of other archetypal TMD compounds, such as the SC $2H$-NbSe$_2$ or the semiconducting $2H$-MoS$_2$; furthermore, the hybridization between H orbitals and the Ti states at the Fermi level is found to be pivotal in reducing the electronic screening and thereby enhance the electron-phonon coupling. Our results establish that the role played by hydrogen in SC layered materials at low pressures is crucial and yet firmly distinct from that found in high-pressure hydrides, providing a key insight for the search of high-temperature superconductivity in layered compounds at ambient pressure.

Results

Electric field-driven hydrogen intercalation. We control the H loading in our $1T$-TiSe$_2$ samples via the ionic liquid gating-induced protonation method[4,6,10,32], as depicted in Fig. 1a. When the gate voltage V_G is swept in ambient conditions above a threshold voltage (Methods), the intense electric field at the TiSe$_2$/electrolyte interface splits the water molecules absorbed in the ionic liquid and drives the H$^+$ ions into the van der Waals gap of the TiSe$_2$ crystal. H incorporation in the TiSe$_2$ lattice is confirmed by nuclear magnetic resonance (NMR) and muon spin rotation (μSR) measurements as discussed later, whereas significant intercalation by the organic ions of the ionic liquid is ruled out via X-ray photoelectron spectroscopy (XPS; see Supplementary Note 1). In-situ monitoring of the room-temperature TiSe$_2$ resistivity during gating (Methods) shows that $\rho(300K)$ remains unaffected by the applied V_G below the threshold for H intercalation, then rapidly decreases and reaches a minimum (Fig. 1b). Maintaining $V_G = +3$ V beyond this point leads to $\rho(300\,K)$ gradually increasing again over time, eventually reaching a plateau for gating times in excess of ~45 min and up to several days.

This gate-induced change in the electric transport properties is non-volatile. Indeed, as shown in Fig. 1c, ex-situ measurements on samples gated for a fixed amount of time and then removed from the electrochemical cell give values of $\rho(300\,K)$ that closely follow those determined in situ. The saturation of $\rho(300\,K)$ for large gating times suggests that most of the H dopants are driven into the sample in the first few tens of minutes, and further increasing the gating time does not alter the average stoichiometry appreciably. This picture is confirmed by assessing the changes to the structural and electronic properties of the protonated samples.

Low-temperature Hall effect measurements (Methods) show an increase in the Hall density n_H at $T = 4.2$ K by more than an order of magnitude, going from ~$4 \cdot 10^{19}$ cm^{-3} in pristine TiSe$_2$ to ~$5 \cdot 10^{20}$ cm^{-3} in H$_2$TiSe$_2$ (Fig. 1d), indicating that H loading introduces a strong electron doping in the protonated TiSe$_2$ samples. At the same time, a room-temperature X-ray diffraction (XRD) analysis (Fig. 1e) shows that the H loading does not alter the $1T$ lattice structure of the pristine material, and simply expands the unit cell by up to ~0.9%. The lattice expansion is comparable to that driven by incorporation of Cu atoms in SC Cu$_x$TiSe$_2$ (~0.6%)[26] and much smaller than the one reported upon lithiation in SC Li$_x$TiSe$_2$ (~12%)[33]. The pronounced broadening of the XRD peaks however indicates that the protonation introduces a large degree of structural disorder in the samples, which may be partially responsible for the re-entrant behavior of $\rho(300\,K)$ upon gating times in excess of those associated to the local minimum shown in Fig. 1b, c. Again, both the structural and the electronic modifications to the TiSe$_2$ crystals occur within the first ~45 min of gating time, confirming the behavior showcased by the room-temperature resistivity.

The dramatic effect of the protonation on the electric transport properties of TiSe$_2$ is even more evident when these are measured as a function of temperature. Fig. 1f shows the temperature dependence of the normalized resistivity $\rho(T)/\rho(300\,K)$ of TiSe$_2$ crystals gated for different amounts of time (Methods). Pristine crystals exhibit a strongly non-monotonic $\rho(T)$ dependence with a broad peak around ~160 K and no sign of a SC transition. This peak is typical of $1T$-TiSe$_2$ and is caused by the reconstruction of the electronic band structure upon the onset of CDW order, which shifts the Fermi level and partially gaps the Fermi
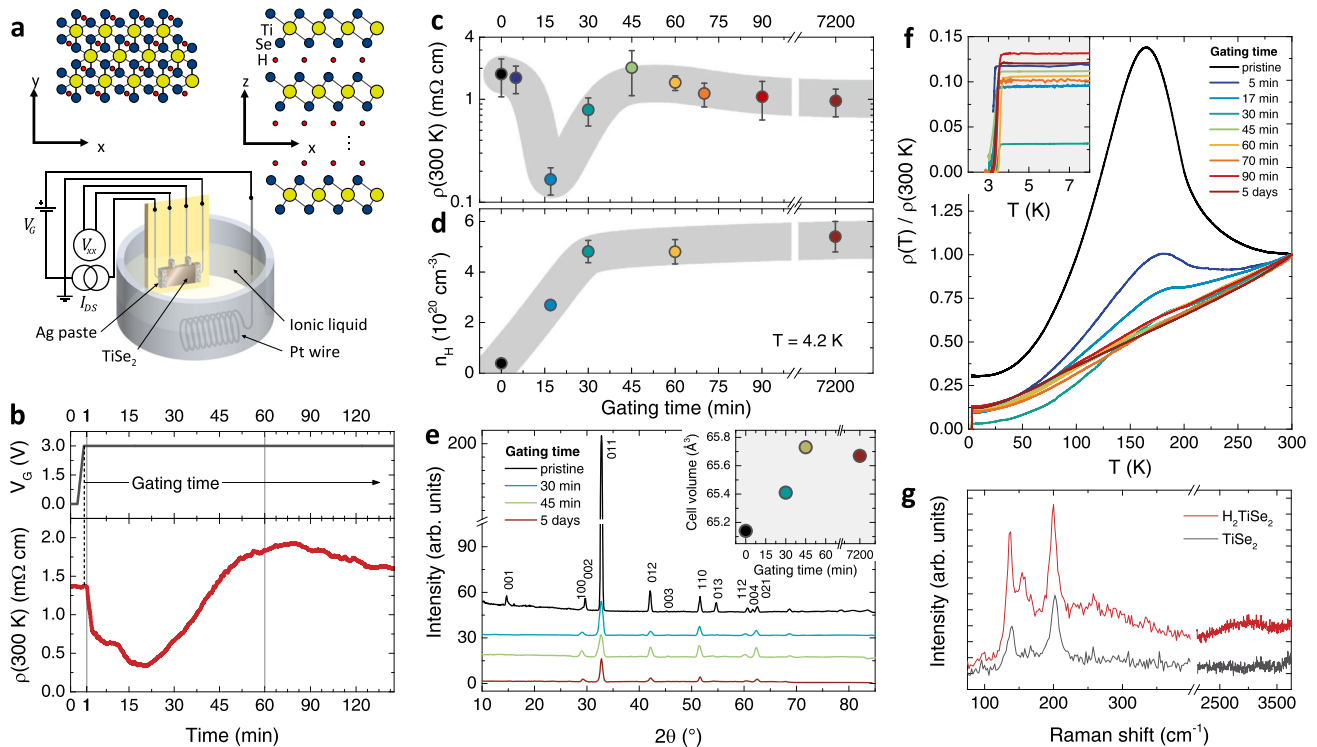
Fig. 1 Ionic liquid gating-induced protonation: electric transport and structural characterization. a Sketch of a TiSe$_2$ crystal immersed in the electrochemical cell for ionic liquid gating-induced protonation, including the electrical connections. The side panel shows a ball-and-stick model of the H$_x$TiSe$_2$ structure with $x \lesssim 1$. **b** Gate voltage V_G and resistivity $\rho(300\,K)$ measured in situ as a function of time, during a typical gating sequence in the electrochemical cell at ambient conditions. The gating time (i.e., the time at which the crystal is kept at $V_G = +3\,V$) is highlighted. **c** $\rho(300\,K)$ measured ex situ and (**d**), Hall carrier density n_H at 4.2 K, of a series of TiSe$_2$ crystals gated for increasing amounts of time. Error bars almost entirely arise from non-ideal sample geometry. Shaded gray bands are guides to the eye. **e** X-ray diffraction spectra in selected TiSe$_2$ crystals at different gating times. The inset shows the resulting unit cell volume as a function of the gating time. **f** ρ as a function of temperature (T) for the same crystals reported in (**c**), normalized by the value at 300 K. The inset shows a magnification of the T range where the superconducting transitions are observed. **g** Raman spectra in ambient conditions acquired on the freshly-cleaved surfaces of a pristine TiSe$_2$ (black curve) and a H$_2$TiSe$_2$ (red curve) crystal.

surface[26,27,30,34,35]. The monotonically-increasing $\rho(T)$ dependence up to T_{CDW} is also commonly observed in high-quality 1T-TiSe$_2$ crystals, but whether it originates from a semimetallic band overlap[36,37] or from a narrow semiconducting gap in the presence of a small extrinsic electron doping[38–40] remains currently uncertain. A small gating time of ~5 min strongly suppresses the intensity of the CDW peak and leads to the appearance of SC with an onset transition temperature $T_c^{on} \simeq 3.3\,K$. Larger gating times up to ~45 min lead to a further reduction in the intensity of the CDW peak and simultaneously slightly increase T_c^{on} to ~3.7 K (with no clear dependence, see inset to Fig. 1f). Also here, gating times in excess of ~45 min lead to a clusterization of the $\rho(T)$ curves around a common behavior, characterized by a complete SC transition with $T_c^{on} \sim 3.7\,K$ and a faint trace of CDW order in the form of a slope change below ~200 K. Consistent with the XRD results, a large degree of structural disorder in these highly-doped samples is evidenced by the four-fold reduction in their residual resistivity ratio (Methods), from its maximum value ~32 attained at a gating time of ~30 min, to a final value ~8 at a gating time of 5 days.

The number of intercalated protons in H$_x$TiSe$_2$ samples pertaining to this state of clusterized $\rho(T)$ and saturated n_H and cell volume (see Fig. 1f, d and e respectively) is quantified by means of ^{1}H-NMR (Methods and Supplementary Note 2). In particular, the decay of the spin-echo amplitude is measured both in a collection of fully-doped TiSe$_2$ crystals and in a reference sample of hexamethylbenzene (C$_{12}$H$_{18}$). A comparison between the signal amplitudes for the two samples shows that the

intercalated TiSe$_2$ crystals contain an average number $x = 2.0 \pm 0.3$ of protons per TiSe$_2$ formula unit. Assuming the H concentration to be linearly proportional to n_H at $T = 4.2\,K$, this then allows estimating an average $x \sim 0.4$ for intercalated TiSe$_2$ to exhibit an incomplete resistive transition with reduced T_c^{on} (gating time of ~5 min), and an average $x \sim 1$ for a complete resistive transition to develop (gating time of ~17 min).

H loading also affects the vibrational properties of TiSe$_2$, as demonstrated by room-temperature Raman spectroscopy on freshly-cleaved surfaces (Fig. 1g; see Methods). Spectra acquired on pristine TiSe$_2$ exhibit the two main Raman modes of 1T-TiSe$_2$, the E$_g$ mode at ~138 cm^{-1} and the A$_{1g}$ mode at ~202 cm^{-1}, consistent with the literature[41–45], and no additional peaks. In spectra acquired on H$_2$TiSe$_2$, the same E$_g$ and A$_{1g}$ peaks are redshifted to ~136 cm^{-1} and ~199 cm^{-1} respectively. Two additional, broader peaks emerge in H$_2$TiSe$_2$ at ~156 cm^{-1} and ~260 cm^{-1}, which could be ascribed to intercalant-activated two-phonon processes at the L and/or M points[42–44,46], and a very broad band appears at high wavenumbers centered around ~2900 cm^{-1}. Our first-principle calculations (see Supplementary Note 3) indicate that the appearance of the peaks at ~156 cm^{-1} and ~260 cm^{-1} can be justified by the removal of symmetry of the 1T-TiSe$_2$ system resulting from the incorporation of H atoms in both atomic (H$_1$TiSe$_2$) and molecular (H$_2$TiSe$_2$) forms. The broad band centered around ~2900 cm^{-1} can instead be naturally interpreted as originating from H$_2$ molecules confined in the TiSe$_2$ matrix, with a renormalized phonon frequency[47,48]. The simultaneous observation of these multiple peaks is therefore

evidence of a strong disorder in the H concentration, phase and distribution in the $TiSe_2$ matrix. In this case, the observation of consistent Raman spectra across different spots in the H_2TiSe_2 crystals could be interpreted as the phase separation between regions with different H concentration to occur over length scales smaller than the laser spot size (~1 μm).

Charge density waves in H_xTiSe_2. The evolution of the CDW order with increasing gating time t can be more accurately tracked by considering its onset temperature, T_{CDW}, and the intensity of the CDW peak, I_{CDW}. As firmly established in the literature[30,33,36], the former can be identified with the position of the inflection point in the $\rho(T)$ curves, that corresponds to the minimum in $d\rho/dT$. As shown in Fig. 2a, which displays $d\rho/dT$ as a function of T, the visibility of the local minimum is suppressed by increasing gating time, but its position remains basically unchanged and close to its pristine value $T_{CDW} \approx 198$ K. The intensity can be evaluated as $I_{CDW} = A_{CDW}(t)/A_{CDW}(0)$, where $A_{CDW}(t)$ is the area contained between each normalized $\rho(T)$ curve (shown in Fig. 1f) and a line connecting its two values at 50 and 250 K[33], as exemplified in Fig. 2d. The trends of T_{CDW} and I_{CDW} as a function of gating time are summarized in Fig. 2b (filled red hexagons and hollow black diamonds, respectively). Clearly, while T_{CDW} is almost constant, I_{CDW} is rapidly suppressed upon increasing gating time, and becomes of the order of 1% of its pristine value in H_2TiSe_2 samples. This behavior is similar to that reported in Li_xTiSe_2 crystals[33], but differs from that of Cu_xTiSe_2[26,49], $Ti_{1+x}Se_2$[37], electrostatically ion-gated $TiSe_2$[30], and $TiSe_2$ under pressure[29], where the suppression of I_{CDW} was accompanied by a decrease of T_{CDW}. The insensitivity of T_{CDW} to increasing doping was interpreted, in the case of Li_xTiSe_2, as a lack of full in-plane percolation of the dopants, leading to a spatial separation between SC Li-rich regions and CDW-ordered pristine regions[33]. The pronounced increase in structural disorder detected by both XRD and Raman spectroscopy in our samples raises the question of whether a similar picture may hold also in the case of H_xTiSe_2.

In general, however, an explanation relying purely on phase separation between H-deficient, CDW-ordered regions and H-rich, SC regions might be too simplistic, since it is not straightforward that the presence of dopants destroys the CDW order in $TiSe_2$ compounds. For example, scanning tunneling microscopy measurements in Cu_xTiSe_2 indicate that CDW order robustly survives even in Cu-rich areas where the local electron doping is large[50,51]. On the other hand, disorder itself is able to suppress the signatures of CDW order in electric transport, as was reported in the case of irradiated $NbSe_2$[52]. In this context, the temperature dependence of the Hall coefficient R_H (Methods and Supplementary Note 4) suggests that a weakened CDW order could survive in dopant-rich areas also in the case of H_xTiSe_2, as shown in Fig. 2d, e. In agreement with the established literature[33,35,36,53], pristine $TiSe_2$ exhibits both a strong CDW peak in $\rho(T)$ (black curve in Fig. 2d, $I_{CDW} \approx 0.9$) and a change of sign in R_H around $T \approx 215$ K (black curve in Fig. 2e). This
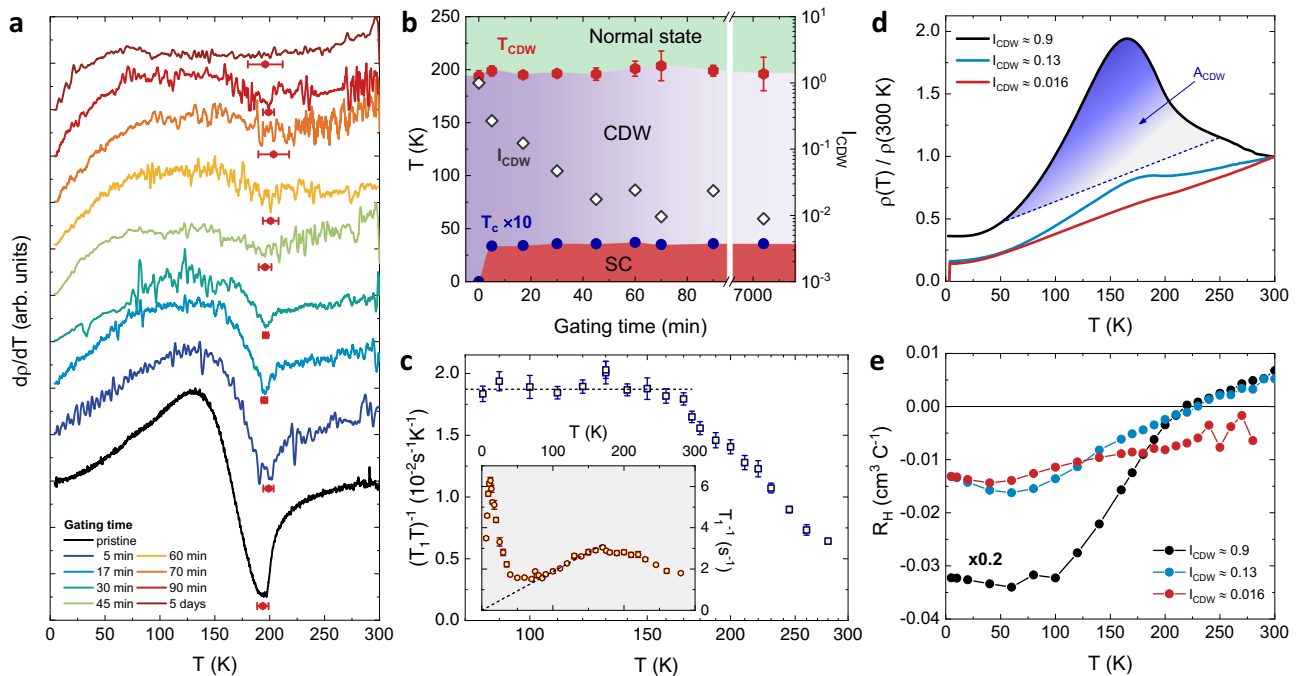

Fig. 2 Charge density waves in H_xTiSe_2. a First derivative of the resistivity ρ as a function of temperature T, $d\rho/dT$, obtained by numerical derivation of the $\rho(T)$ curves shown in Fig. 1f for increasing gating time. Red hexagons highlight the temperature T_{CDW} at which the local minimum associated with the onset of CDW order is observed. Error bars show the uncertainty on its determination due to the experimental noise level. **b** Temperature-gating time phase diagram of H_xTiSe_2. The onset temperature of CDW order, T_{CDW}, and the superconducting transition temperature, T_c, are plotted as a function of gating time (left scale). The CDW intensity I_{CDW} (right scale) is calculated as $A_{CDW}(t)/A_{CDW}(0)$, where $A_{CDW}(t)$ is the area contained between each normalized resistivity curve, $\rho(T)/\rho(300$ K), and a straight line connecting the data points at 50 and 250 K. Shaded areas highlight the different phases observed in the system. **c** T dependence of the spin-lattice relaxation rate T_1^{-1} at $\mu_0 H \simeq 3.5$ T (inset). The dashed line is a linear fit to the experimental data highlighting a well-defined Korringa-like behavior for $T \lesssim 170$ K and a marked decrease of T_1^{-1} upon increasing temperature above 210 K. The main panel reports the T dependence of $(T_1 T)^{-1}$, making the crossover between the different behaviors even clearer. The dashed line is a constant line corresponding to the fitting curve reported in the inset. Error bars are the standard deviation of the fit parameters in Eq. (3). **d** Normalized resistivity and (**e**), Hall coefficient R_H as a function of T in three $TiSe_2$ crystals with different I_{CDW}. Both protonated crystals (intermediate and low I_{CDW}) are superconducting with $T_c^{on} \approx 3.7$ K, which is defined as the threshold where $\rho(T)$ reaches 95% of its normal-state value. The shaded blue region in (**d**) highlights the area from which $A_{CDW}(t)$ is calculated.

occurs when the onset of CDW order opens a gap at the Fermi level in part of the band structure, causing a reconstruction in the Fermi surface which changes the dominant character of the charge carriers from holonic for $T \gtrsim T_{CDW}$ to electronic for $T \lesssim T_{CDW}$[33,35,36,53]. An intermediate H doping (blue curve in Fig. 2d, e) suppresses the CDW peak in $\rho(T)$ ($I_{CDW} \approx 0.13$) and strongly reduces the absolute value of R_H, but a sign change is still clearly present at $T \approx 225$ K, indicating that the Fermi surface still undergoes a reconstruction. H_2TiSe_2 alone (red curve in Fig. 2d, e) exhibits no sign change in R_H up to ~300 K, and a CDW peak in $\rho(T)$ reduced to a slope change ($I_{CDW} \approx 0.016$). However, the Hall coefficient remains strongly T-dependent, resulting in a tenfold reduction in n_H as the sample is cooled from 300 to 4 K. This freeze-out of the free charge carriers can be ascribed to the presence of trap states introduced by structural disorder, but could also be assisted by a residual partial gapping of the Fermi surface if a weakened CDW order survives in the H-rich regions. The absence of a sign change in R_H could indicate either that the CDW gap still opens around ~200 K in H_2TiSe_2 but is partially shifted below the Fermi level by the increasing electron doping (similar to the case of Cu_xTiSe_2[50,51]), or that the disorder introduced by the H intercalation suppresses long-range CDW order in the H-rich regions and allows only short-range CDW order to survive (as in the case of irradiated $NbSe_2$[52]). A combination of the two effects is of course also possible.

Strong indications of a reconstruction of the Fermi surface around $T \sim 200$ K are also obtained from NMR measurements of the ^1H spin-lattice relaxation rate T_1^{-1} in H_2TiSe_2 samples at $\mu_0H \simeq 3.5$ T (Methods). As shown in the inset to Fig. 2c, T_1^{-1} exhibits a linear dependence on T for 80 K $\lesssim T \lesssim 170$ K consistent with the so-called Korringa behavior proper of relaxation processes mediated by itinerant electrons[54]. This is in agreement with the results of NMR measurements in other TMDs such as VSe_2, VS_2, and $IrTe_2$ within the CDW phase[55–57]. Higher temperatures $T \gtrsim 170$ K mark a clear departure from the linear-in-temperature trend. In particular, a plateau of T_1^{-1} between 170 and 210 K is followed by a suppression of T_1^{-1} upon increasing T. The crossover between the two different behaviors is even clearer in the T dependence of $(T_1T)^{-1}$ (main panel of Fig. 2c) and it seemingly correlates with the onset of the CDW phase. In the ideal case of a Fermi gas, it is well-known that $(T_1T)^{-1} \propto \varrho(E_F)$ – i.e., the density of states at the Fermi energy[54]. The observed drop of $(T_1T)^{-1}$ for $T \gtrsim 170$ K is then strongly indicative of a progressive decrease of $\varrho(E_F)$ upon increasing temperature above the critical temperature of the CDW phase, at variance with what is observed in VSe_2, VS_2, and $IrTe_2$[55–57]. This peculiar behavior will be discussed in detail elsewhere[58]. Finally, we stress that the sharp maximum observed in the spin-lattice relaxation rate at around 10 K has already been reported in pristine $TiSe_2$[59]. This observation confirms that the intercalated ^1H nuclei probe the intrinsic electronic properties of the host material.

Superconductivity in H_xTiSe_2. The evolution of the SC phase in H_xTiSe_2 appears completely unaffected by the presence of CDW order, as summarized by the values of T_c as a function of gating time (blue circles in Fig. 2b). A complete SC transition with a sizeable $T_c^{on} \sim 3.7$ K is observed not only in the fully-doped H_2TiSe_2, where no Fermi-surface reconstruction is detected by Hall effect, but also in the partially-doped H_xTiSe_2, where the Fermi surface is certainly partially gapped (see inset in Fig. 1f). In a magnetic field μ_0H perpendicular to the ab plane of the H_2TiSe_2 crystal (Fig. 3a and Supplementary Note 5; see Methods) the SC transition broadens and shifts to lower T. At 2 K, a well-defined zero-resistance state (ZRS) is observed at least up to $\mu_0H = 30$ mT and the intermediate dissipative regime exhibits the typical

behavior of a thermally-activated flux flow (TAFF), $\rho(T, H) = \rho_0 \exp[-U(H)/k_B T]$, at any T and H. This is clear from Fig. 3b, where ρ/ρ_0 is plotted in logarithmic scale against T^{-1}. The activation barrier for vortex motion, obtained from these curves, scales logarithmically with increasing magnetic field, $U(H) = U_0 \ln(B_0/\mu_0H)$ (right panel in Fig. 3b), indicating a collective flux creeping[60]. A fit to the $U(H)$ data gives $U_0 \approx 8.9$ meV and $B_0 \approx 0.39$ T, comparable to the values found in ion-gated $TiSe_2$[31]. The observation of this direct transition from ZRS to TAFF already at relatively large $T \gtrsim 2$ K is analogous to those found in overdoped Li_xTiSe_2[33] and Cu_xTiSe_2[26], and provides no evidence that H_xTiSe_2 may host the anomalous quantum metallic behavior that was claimed to destroy the ZRS at arbitrarily small magnetic fields in ion-gated $TiSe_2$[31] and in under- and optimally-doped Li_xTiSe_2[33].

Figure 3c shows the T-dependence of the zero-field cooled (ZFC) magnetic moment $m(T)$ measured below ~5 K at $\mu_0H = 1$ mT (Methods). A rather sharp transition is observed at $T_c^{on} = 3.6 \pm 0.1$ K, in reasonable agreement with the T_c value determined by transport measurements. As expected for the Meissner state, the isothermal $m(H)$, measured at $T = 2$ K following a ZFC procedure, decreases linearly with increasing H, up to 1.3 ± 0.3 mT (Fig. 3d). Above this field, $m(H)$ starts deviating from a linear dependence, thus defining the lower critical field $H_{c1}(2$ K$)$. Upon further increasing H, $m(H)$ first reaches a minimum at ≈ 5.8 mT and then it decreases in modulus, returning to zero at the upper critical field $\gtrsim 100$ mT, in fairly good agreement with the $H_{c2}(T)$ value determined from transport measurements (where we use the criterion of 95% normal-state resistivity).

By combining the resistivity- and magnetization measurement results, we can construct the SC T–H phase diagram of H_2TiSe_2 shown in Fig. 3e. The Meissner state exists for magnetic fields $H \lesssim H_{c1}$, above which SC vortices penetrate the sample volume and move in the TAFF regime until $H = H_{c2}$, here defined as the field where ρ reaches 95% of its normal-state value. The T-dependence of H_{c2} shows a prominent kink around ~$0.85T_c$, where its slope changes abruptly from ≈ -0.23 to ≈ -0.13 T/K. These two slopes correspond to an in-plane coherence length $\xi_{ab}(0)$ of 26 and 20 nm, respectively (Methods). We note that, as shown in Fig. 3e, this behavior is invariably observed across all the measured H_2TiSe_2 samples with little sample-to-sample variation, even in those that exhibit a strongly biphasic resistive transition (Supplementary Fig. 6a) or a weakly-localized normal state (Supplementary Fig. 6b). This indicates that it is mostly insensitive to disorder and sample inhomogeneities, and therefore is likely an intrinsic property of the material. As a consequence, since this feature deviates considerably from the single-band mean-field behavior exhibited by both the 3D Cu_xTiSe_2 and the ion-gated 2D $TiSe_2$, it suggests that H_xTiSe_2 may be a multi-band superconductor, where it is instead commonly observed[61–63].

Further insight into the SC properties of the H_2TiSe_2 is obtained by transverse-field (TF) μSR measurements[64,65] (Methods and Supplementary Note 6). Figure 4a, b show the zero-field cooling (ZFC) TF-polarization curves recorded either in an applied field parallel to the ab-planes, $\mu_0H = 14$ mT, or parallel to the c-axis, $\mu_0H = 10$ mT. As to the former (panel a), no significant differences were detected between datasets taken at $T = 0.28$ K and $T > T_c$. For fields applied parallel to the c-axis, instead, clearly distinct datasets are observed in the SC- and the normal state. The volume fraction of those muons probing the vortex state, f_{sc}, was determined by fitting the time-dependent TF polarization data by using a two-step calibration procedure [see details in Methods and Eq. (4)]. We find a lower limit for the SC volume fraction $f_{sc} = 44 \pm 1\%$, thus confirming the bulk nature of H_xTiSe_2
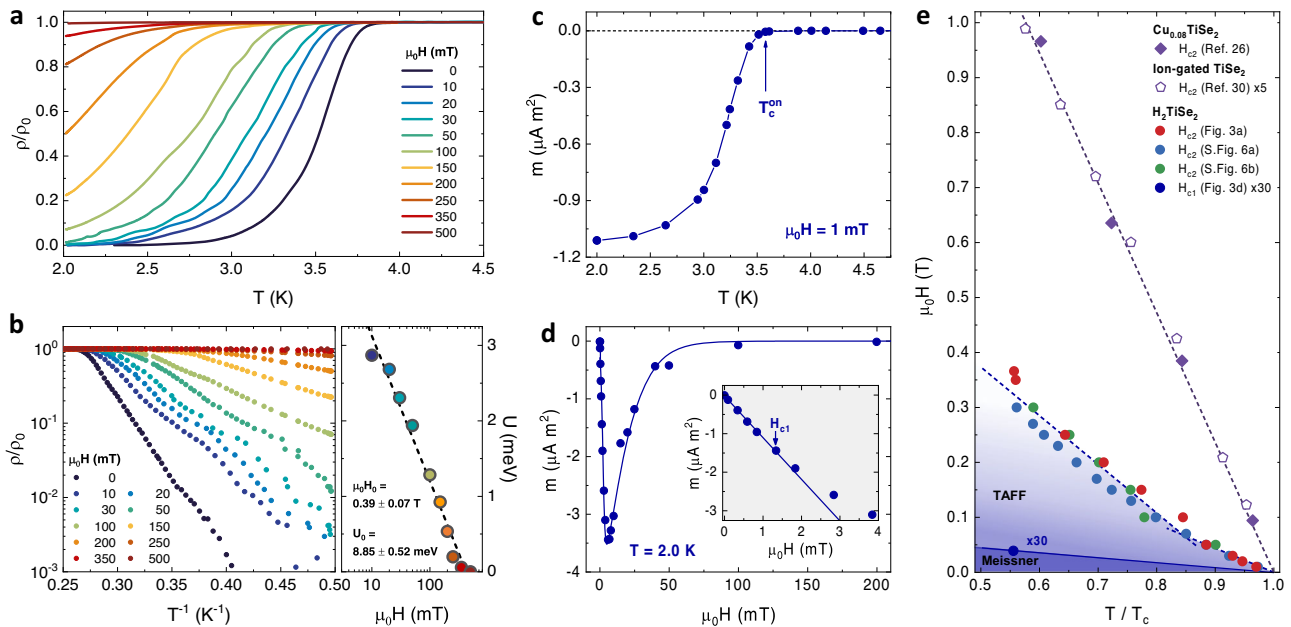
Fig. 3 Magnetotransport and magnetization of superconducting H_2TiSe_2. a, Resistivity ρ of a H_2TiSe_2 crystal as a function of temperature T in the superconducting transition, normalized by its normal-state value ρ_0, for increasing magnetic field H applied orthogonal to the crystal ab plane. **b**, Same data of **a** plotted in semilogarithmic scale as a function of T^{-1}, highlighting the Arrhenius behavior characteristic of thermally-activated flux flow (TAFF). The side panel shows the TAFF activation energy U as a function of μ_0H. Dashed black line is the linear fit to the data in semilogarithmic scale which allows determining the characteristic energy U_0 and magnetic field μ_0H_0. **c**, T-dependence of the magnetic moment m, recorded under zero-field cooling (ZFC) conditions with $\mu_0H = 1$ mT magnetic field applied perpendicular to the ab plane. The arrow indicates the T below which the magnetic moment starts deviating from its normal-state value, thus defining the diamagnetic onset temperature $T_c^{on} = 3.6 \pm 0.1$ K. **d**, ZFC magnetic moment as a function of H measured isothermally at $T = 2$ K. The line is a guide to the eyes. The inset shows a magnification of the low-field region, with a linear fit on the first six points (line). The arrow indicates the field above which the magnetic moment starts deviating from a linear dependence, thus defining the first critical field $H_{c1} = 1.3 \pm 0.3$ mT. **e**, $H - T$ phase diagram of H_2TiSe_2 constructed by combining the results from resistivity and magnetization measurements on multiple different crystals. Shaded blue regions highlight the Meissner state and the TAFF state. Red and indigo circles are obtained from the data shown in **a** and **d** respectively. Blue and green circles are obtained from Supplementary Fig. 6a and b respectively. Dashed blue lines are linear fits to the resistive critical magnetic field H_{c2} (defined as the threshold for reaching $\rho(T) = 0.95\rho_0$) above and below the kink at $T/T_c \approx 0.85$. The resistive H_{c2} data for Cu_xTiSe_2[26] and ion-gated $TiSe_2$[30] are shown for comparison.

superconductivity, leaving however open the possibility that some sample regions may still be normal, as expected in case of an inhomogeneous distribution of H dopants.

In the ZFC case, the temperature dependence of the in-plane Gaussian depolarization rate of the implanted muons $\sigma(T)$, resulting from fits to Eq. (4) (Methods), is shown in Fig. 4c. It includes the contributions of σ_n and σ_{sc}, the depolarization rates in the normal and SC state, respectively, and is given by $\sigma = \sqrt{\sigma_n^2 + \sigma_{sc}^2}$. σ_n is due to the contribution of the randomly-oriented nuclear dipole moments, here fully dominated by the intercalated H nuclei, whose moments are only partially quenched by the applied magnetic field. Therefore, the observation of a finite $\sigma_n = 0.32 \pm 0.02$ μs^{-1} in the normal state (dashed line in Fig. 4c) provides an independent confirmation of the sizeable H intake in the H_2TiSe_2 samples. The effective magnetic penetration depth was estimated by measuring also a TF spectrum at base T (dark-blue square in Fig. 4c), now using a standard field-cooling (FC) procedure, which provides a SC-depolarization rate $\sigma_{sc} = 0.14 \pm 0.03$ μs^{-1} at $T = 0.28$ K. This, in turn, implies a rather large value for the in-plane magnetic penetration depth, $\lambda_{ab} = 900 \pm 100$ nm (Methods), indicative of a low superfluid density. Furthermore, the T dependence of σ does not show any signs of saturation down to the lowest temperature (0.28 K). At the same time, auxiliary zero-field measurements confirm that time-reversal symmetry is preserved in H_2TiSe_2 (see Supplementary Note 7). This result suggests that H_2TiSe_2 hosts a gapless-like SC state, thus making future spectroscopic

investigations of the symmetry of SC gap(s) of this material highly desirable.

Density functional theory of H_xTiSe_2. The effects of H intercalation on the structural, electronic and SC phase of $1T$-H_xTiSe_2 were investigated from a theoretical standpoint by means of ab initio density functional theory (DFT) calculations (Methods and Supplementary Note 8). Simulations based on a random-search algorithm reveal the existence of several metastable intercalation sites for H in the $1T$-$TiSe_2$ lattice, indicating that it can easily be trapped (at $T = 0$) in different local energy minima. In particular, for concentrations up to x $\lesssim$ 1 H preferentially sits in the van der Waals gap at the bridge position between two Se atoms belonging to different planes (Fig. 5a).

From the electronic standpoint, for x $\lesssim$ 0.1 H acts as an electron donor, rigidly shifting the Fermi level in the conduction band of $TiSe_2$ where the electronic states exhibit a predominant in-plane character (Supplementary Fig. 10a). The simple rigid-band-shift picture breaks down at intermediate concentrations (x $\approx$ 1), where H doping leads to a strong deformation of the intrinsic electronic dispersion of $1T$-$TiSe_2$ (shown as the gray curve in Fig. 5b), induces a sizeable hybridization between the $TiSe_2$ bands and the H-derived orbitals, and completely switches the orbital character of the bands which cross the Fermi level (Fig. 5b, red curve). Indeed, the positive potential induced by the ionized H atoms in the van der Waals gap of $1T$-$TiSe_2$ lowers the energy of the bands with orbital character extending in the inter-
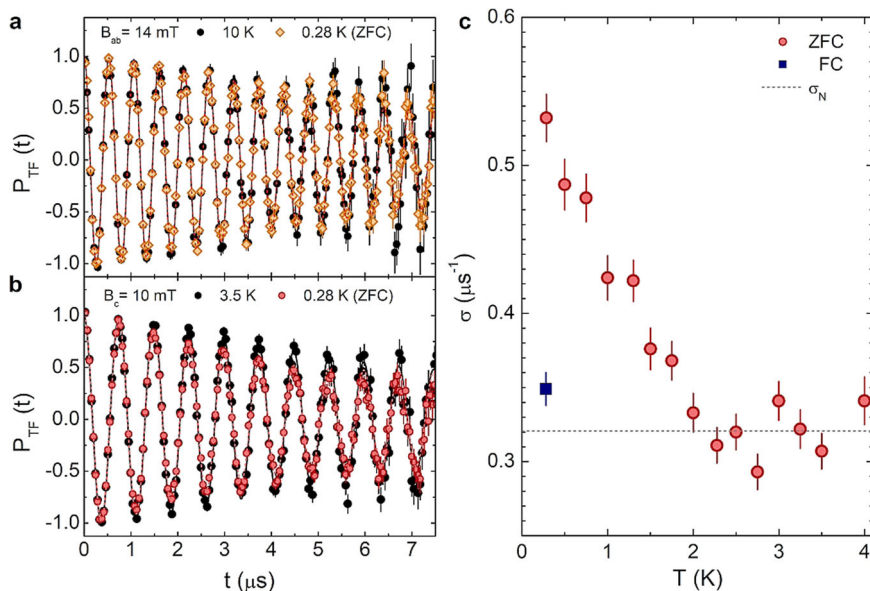
Fig. 4 Muon spin rotation in superconducting H_2TiSe_2. a, **b** Zero-field cooling transverse-field muon-spin polarization $P_{TF}(t)$ in a 14-mT magnetic field applied parallel to the *ab* planes, (**a**), or in a 10-mT field applied parallel to the *c*-axis, (**b**). Solid lines are fits to the model described by Eq. (4). The error of the positron count for each bin is its standard deviation, while the error bars of each bin in $P_{TF}(t)$ are calculated by error propagation. **c** Temperature dependence of the depolarization rate (red circles) in a magnetic field $\mu_0 H = 10$ mT, applied parallel to the *c* axis. Note the lack of saturation at low temperatures. The dark-blue square represents the depolarization rate recorded after field cooling in the same applied magnetic field. The gray dashed line represents the average nuclear dipolar contribution, here, $\sigma_n = 0.32 \pm 0.02$ μs^{-1}. The error bars are the standard deviation of the fit parameters.
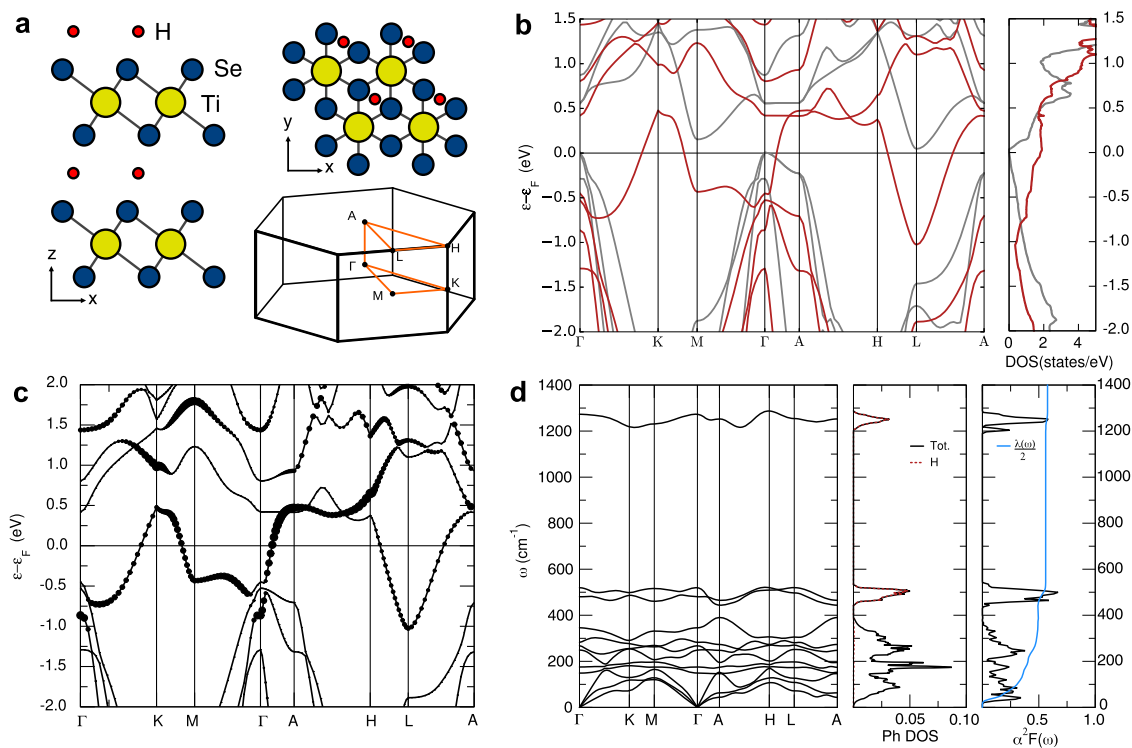

Fig. 5 First-principles electronic and phononic structures of H_xTiSe_2. a Ball-and-stick model of the protonated $1T$-$TiSe_2$ structure in the ground-state adsorption site with one H atom placed in the van der Waals gap at the Se-Se bridge position (also shown in Fig. 1a). The Brillouin zone with high symmetry points is also shown. **b** Electronic band structure and density of states of $1T$-H_1TiSe_2 in the structure shown in panel (**a**) (red) compared with the pristine $1T$-$TiSe_2$ dispersion (gray). **c** Orbital character of the electronic band structure of $1T$-H_1TiSe_2, with the d_{z^2} character of the bands indicated by the size of the black circles. **d** Phonon dispersion relations (left panel), density of states (central panel), and electron-phonon spectral function $\alpha^2 F(\omega)$ (right panel) of pressurized $1T$-H_1TiSe_2. The spectral contributions of the H-derived modes are highlighted as red dashed lines. The right panel also reports the frequency-dependence of the total electron-phonon coupling $\lambda(\omega)$ as a solid blue line.

layer gap, like the d_{z^2} band (the intensity of which is depicted as solid circles in Fig. 5c). This band structure engineering is crucial for the development of SC order, since the d_{z^2} character of the states at the Fermi energy was already found in the SC TMD compounds NbS$_2$ and NbSe$_2$, where the d_{z^2} bands are partially-filled[66–68].

Conversely, a further increase in doping level, to the concentration determined in fully-doped H$_x$TiSe$_2$ samples by NMR ($x \approx 2$), leads to the emergence of two possible phases. One is characterized by the formation of H$_2$ molecules in the van der Waals gap and a band structure akin to that of intrinsic 1T-TiSe$_2$ (Supplementary Fig. 10b). The other is a metastable insulating phase, achieved when the stoichiometry is exactly 2 H atoms per unit cell (Supplementary Fig. 10d). The actual H$_x$TiSe$_2$ samples are likely to be characterized by a strong disorder in the distribution of H atoms, and will thus exhibit a mixture of different single phases which however all turn out to be dynamically unstable (see Supplementary Note 8 for further details). This in turn prevents a full ab-initio calculation of the properties of the real system, in particular for the calculation of the SC critical temperature.

To have solid first-principles predictions of the SC phase even in the high density regime, the metallic 1T-H$_1$TiSe$_2$ phase was therefore artificially stabilized by slightly reducing the lattice constants by 4% (that corresponds to an external pressure of ~10 GPa, see Methods). This approach, already exploited to remove the CDW distortion in pure 1T-TiSe$_2$[69] and reduce anharmonic effects in H-doped palladium alloys[70], allows obtaining a dynamically stable high-doping phase while at the same time leaving the main features of the electronic properties of 1T-H$_1$TiSe$_2$ mostly unaffected (as shown in Supplementary Fig. 11). The resulting phonon band structure shows the appearance of H-derived branches (highlighted in red in the phonon density of states shown in Fig. 5d), comprising a high-energy band around 1300 cm^{-1} and more entangled branches at lower frequencies, close to the TiSe$_2$ modes around 500 cm^{-1}. Overall, the pressurized H$_1$TiSe$_2$ phase is therefore able to mimic all the key modifications introduced by the H dopants in the real TiSe$_2$ samples.

In particular, the dynamical stability of the pressurized H$_1$TiSe$_2$ structure allows computing the electron-phonon spectral function $\alpha^2 F(\omega)$, shown in Fig. 5d, from which both the electron-phonon coupling λ and the SC T_c can be determined (Methods). In sharp contrast with the high-pressure hydrides[32,71], the H-derived phonon branches do not sensibly contribute to the total coupling $\lambda = 1.15$, which is however found to be significantly higher with respect to that of the low-doping structure ($\lambda = 0.5$, see Supplementary Note 8). As a consequence, H$_1$TiSe$_2$ is predicted to become SC at $T_c \sim 13$ K (Methods), a critical temperature surely higher than the experimentally-measured one, but of the same order of those measured in other SC TMDs[15,67,68]. This overestimation can be ascribed to differences between the real material and the computational model, with disorder effects and doping inhomogeneities easily lowering the real T_c with respect to the ideal case considered in the calculations. Anyway, the much larger predicted T_c with respect to that of the low-doping structure ($T_c \sim 1.5$ K, see Supplementary Note 7) highlights the crucial role played by the H dopants in determining the properties of the SC phase. Note that this enhancement cannot be ascribed merely to the application of pressure to the TiSe$_2$ structure, since the T_c of undoped 1T-TiSe$_2$ at 10 GPa is $\ll 1$ K[29,69].

Discussion

Our results show that ionic liquid gating-induced protonation allows for a robust and non-volatile tuning of the electronic ground state of archetypal correlated layered compound 1T-TiSe$_2$. We demonstrate that this tuning is qualitatively different from what is obtained by other doping methods, such as electrostatic gating and Cu or Li intercalation. An increased level of hydrogen doping suppresses the intensity of the CDW phase of undoped TiSe$_2$ and triggers the onset of superconductivity. Still, vestigial traces of the CDW ordering, observed even in H$_2$TiSe$_2$—a stoichiometry unattainable via Li or Cu intercalation—hint at the coexistence of both phases in a wide doping range. This coexistence is likely enabled by the strongly disordered nature of the hydrogen-rich compound, which hosts a mixture of different phases with distinct electronic structures determined by the several possible hydrogen intercalation configurations. The observed SC phase, possibly gapless and multi-band in character, together with the absence of an anomalous metallic phase are also at odds with what is reported in other SC TiSe$_2$ compounds. Our experimental results are consistent with ab initio calculations showing how the effect of H intercalation is not limited to a rigid-band doping, but can lead to a full band-structure engineering of the undoped TiSe$_2$ compound. The role of hydrogen is crucial in determining the emergence of superconductivity through different mechanisms: (i) at low concentrations, H intercalation rigidly charge-dopes the system, weakening the CDW ordering and increasing the electron–phonon coupling at the Fermi level; (ii) at higher concentrations, the doping mechanism changes, triggering a band inversion that cannot be described within a rigid band shift; this leads to the partial filling of the highly-coupled d_{z^2} band, mimicking the exact band population found in Nb-based transition-metal dichalcogenides of the 2H polytype, such as 2H-NbSe$_2$ and 2H-NbS$_2$, which are superconductors even without doping; (iii) H intercalation also induces the hybridization of these d_{z^2} states with H-derived orbitals, reducing the screening of the phonon perturbations and thereby further increasing the electron-phonon coupling. This clearly indicates that the SC phase realized in H$_x$TiSe$_2$ should be of a different nature with respect to those observed in Cu$_x$TiSe$_2$ or in electron-doped MoS$_2$, reflecting the different orbitals involved in the electron–electron pairing and the capability of H doping to hybridize the electronic states at the Fermi level and reduce the screening to phonon perturbations. At the same time, its origin is firmly distinct from that found in high-pressure hydrides, since in H$_x$TiSe$_2$ the high-frequency phonon spectral contributions due to the light H atoms remain weakly coupled to the electronic states at the Fermi level.

In summary, our findings show ionic liquid gating-induced protonation to be a unique doping technique, distinct from the more ubiquitous chemical substitution and alkali intercalation. Furthermore, the understanding of the difference between the mechanisms at play in hydrogen-rich superconductors at mega-bar pressures[71] and in H$_x$TiSe$_2$ will be crucial in the quest for new high-T_c superconductors at ambient and low pressures, as also suggested by the room-temperature superconductivity recently claimed to appear in lutetium hydride at relatively low pressures[3]. Gate-driven protonation will enable accessing new electronic phases of the host compounds at ambient pressure, where hydrogen not only injects high-frequency phonon spectral contributions, but can play a triple role as a charge dopant, a source of band-selective filling, and a knob to tune the electronic screening via orbital hybridization.

Theoretical proposals in hydrogen-doped systems are recently appearing, confirming our experimental and theoretical analysis. All studies highlight how superconductivity can be induced in different materials by hydrogen incorporation. Among others, we cite the hydrogen-induced SC phases in PdCu[70], diborides like MgB$_2$[72] and TiB$_2$[73], chromium[74], Mo$_2$C$_3$[75], hBN[76], and in carbon nanostructures[77]. The experimental realization of these theoretical proposals, made possible by the simple and reliable

technique shown in this work, can reverse the accepted paradigm to access high-temperature SC phases of hydrides from the high-pressure side. Here we propose an alternative route for stabilizing new hydrogen-rich compounds, starting from promising materials at ambient pressure, driving them to the predicted SC state and then, eventually, further enhancing their SC properties by applying low or moderate pressures.

Methods

Ionic liquid gating-induced protonation. Freshly-cleaved 1T-TiSe$_2$ crystals (HQ Graphene; typical size $1.0 \times 0.5 \times 0.05$ mm^3) were electrically contacted by drop-casting small droplets of silver paste (RS Components) to thin gold wires and immersed in a Duran crucible (40 mm diameter) filled with 1-ethyl-3-methylimidazolium tetrafluoroborate ionic liquid (EMIM-BF$_4$, Sigma Aldrich) together with a platinum (Pt) counter electrode. The gate voltage V_G was applied to the Pt electrode at 300 K in ambient atmosphere by an Agilent B2961 power source. The applied V_G was always limited to a maximum value of $+3$ V and the gating temperature to 300 K so as to avoid undesired electrochemical reactions between the sample and the ionic liquid such as sample etching[78] or organic-ion intercalation[79]. The four-wire resistance $R = V_{xx}/I_{DS}$ was monitored in situ by sourcing a constant current $I_{DS} \approx 100$ μA between the outer drain (D) and source (S) contacts with a Keithley 220 current source, and measuring the longitudinal voltage drop V_{xx} between the inner voltage contacts with an HP3457 multimeter. The resistivity was then determined as $\rho = Rtwl^{-1}$, where t and w are the sample thickness and width, and l is the distance between the inner voltage contacts. Common-mode offsets were removed using the current-reversal method. The protonated TiSe$_2$ samples were then extracted from the cell and rinsed with acetone and ethanol to remove ionic-liquid residues before further ex-situ characterization. In between measurements, samples were stored in standard desiccators either under low vacuum or in argon atmosphere to avoid moisture contamination.

Electric transport measurements. All protonated TiSe$_2$ crystals discussed in this work were characterized via ex-situ temperature-dependent resistivity measurements carried out in the high-vacuum chamber of a Cryomech pulse-tube cryo-cooler with a base temperature of ≈ 2.8 K. The magnetotransport properties of selected crystals were measured either up to ≈ 4.5 K in the variable-temperature insert of a ^{4}He Oxford cryostat, or up to ≈ 300 K in a Quantum Design physical properties measurement system (PPMS), both equipped with 9 T SC magnets. The resistivity was determined as in the room-temperature gating runs, except that the source-drain current was sourced via an Agilent B2912 source-measure unit (Oxford cryostat) or using a standard 4-probe technique with the Resistivity option for the PPMS. The user bridge board of the PPMS has a digital-to-analog converter (DAC) which adjusts the excitation current and a delta-sigma A/D converter which reads the voltage output. In AC mode, the user bridge board applies a DC excitation to the sample and at each measurement it reverses the current averaging the absolute value of the positive and negative voltage readings. This operation eliminates errors from DC offset voltages and produces the most accurate readings. Both the longitudinal (V_{xx}) and transverse (V_{xy}) voltage drops were measured via an Agilent 34420 nanovoltmeter (Oxford cryostat) or by means of a standard 6-terminal method with the Resistivity option for the PPMS. The magnetic field H was always applied orthogonal to the samples' ab plane.

The Hall coefficient was determined from the antisymmetrized $R_{xy} = V_{xy}/I_{DS}$ data as:

$$R_H = \frac{t}{\mu_0} \times \frac{dR_{xy}(T)}{dH} \tag{1}$$

and the Hall density was calculated as $n_H = (eR_H)^{-1}$ where e is the elementary charge.

In SC samples, the residual resistivity ratio was determined as $\rho(300\,\mathrm{K})/\rho_0$, where ρ_0 is the resistivity value in the normal state immediately above the SC transition; the onset transition temperature T_c^{on} was determined as the threshold where $\rho(T)$ reaches 95% of ρ_0; and the zero-temperature in-plane coherence length was determined as:

$$\xi_{ab}(0) = \sqrt{\frac{\Phi_0/2\pi}{-\mu_0(dH_{c2}/dT)\,T_c^{on}}} \tag{2}$$

where H_{c2} is the magnetic field at which $\rho(H)$ reaches 95% of its normal-state value, μ_0 is the vacuum permeability, dH_{c2}/dT is the slope of the $H_{c2} - T$ curve, and Φ_0 is the magnetic flux quantum.

X-ray diffraction. X-ray powder diffraction patterns of the TiSe$_2$ samples were collected ex situ on selected single crystals after thorough removal of the ionic liquid residues and of the electrical leads using a 114.6 mm Gandolfi camera, with Ni-filtered Cu K-α radiation source and an exposure time of 48 h. Diffraction was impressed on a photographic film and reduced using the software X-RAY[80] to obtain the intensity profiles as a function of the diffraction angle.

Raman spectroscopy. Raman spectra were acquired on freshly-cleaved surfaces in ambient conditions using a Renishaw InVia H43662 micro-Raman spectrometer. All spectra were acquired using an excitation wavelength of 514 nm, a laser power <1 mW focused through a 100X objective, an exposure time of 20 s, and 50 accumulations.

Nuclear magnetic resonance. ^{1}H-NMR measurements at $\mu_0H \simeq 3.5$ T (magnetic field parallel to the crystallographic ab plane) were performed using a TecMag Apollo spectrometer coupled to a resonant circuit made of an in-series combination of a 470 pF capacitor and of a seven-loop solenoidal coil. The coil was deformed in order to mimic the flake-like shape of the crystals and to maximize the geometrical filling factor, in turn. The spin-lattice relaxation time T$_1$ was quantified via a conventional inversion-recovery pulsed sequence. In particular, T_1^{-1} was extracted based on a best-fitting of the experimental recovery curves based on a stretched-exponential function

$$M(\tau) = M(\infty)\left\{1 - 2f\exp\left[-\left(\frac{\tau}{T_1}\right)^\beta\right]\right\}. \tag{3}$$

Here, $M(\tau)$ is the component of the nuclear magnetization along the quantization axis at time τ after the first inversion radio-frequency pulse, $M(\infty)$ is the equilibrium magnetization, $f \leq 1$ allows for non-ideal inversion conditions and β is the stretching exponent. $\beta \sim 0.9$ was quantified independently on temperature, in good agreement with the purely-exponential behavior expected for spin-1/2 nuclei.

Magnetization measurements. Systematic measurements of the magnetic moment as a function of temperature and magnetic field were carried out on a small H$_2$TiSe$_2$ single crystal with approximate surface ~ 1 mm^2 by means of a SC quantum interference device (SQUID) magnetometer. Since the sample mass was less than 0.1 mg (i.e., below the sensibility threshold of a standard laboratory balance), the magnetic field had to be applied perpendicular to the sample surface (i.e., to ab planes). Such setup maximizes the effects of the demagnetizing factor, thus enhancing the diamagnetic signal in the SC state. The unavailability of a reliable value for the sample mass (or volume) prevents us from providing an accurate estimate of the shielding fraction in the SC state.

Muon-spin rotation measurements. Muon-spin rotation (μSR) is an extremely sensitive probe of the local (i.e., microscopic) electronic properties, which uses spin-polarized positive muons implanted in the sample under test[64,65]. Depending on the material density, muons typically penetrate over a depth of several hundreds of microns and, thus, are implanted homogeneously over the whole sample volume. Because of this, muons are considered as a bulk probe of matter. All the μSR measurements were carried out at the Dolly spectrometer (πE1 beamline) of the Swiss Muon Source at the Paul Scherrer Institute, Villigen, Switzerland. A ^{3}He cryostat was used to reach temperatures down to 0.28 K. A mosaic of H$_2$TiSe$_2$ single crystals is glued using GE-varnish on a 25-μm thick copper foil, here acting as a thermal link (Supplementary Fig. 7). A 100-μm-thick high-purity silver degrader was fixed in front of the sample. All measurements were performed using an active veto scheme, thus removing the background signal due to muons which miss the sample. μSR measurements were performed following both standard FC and nonstandard ZFC protocols. In the former case, a regular lattice of vortex lines is established over the sample volume. This is a key requirement in order to accurately determine the magnetic penetration depth and the superfluid density. In the ZFC case, instead, we induce an artificially disordered vortex lattice in the SC state that, in turn, causes highly inhomogeneous local magnetic fields at the implanted muon sites and, hence, a much higher muon-spin depolarization rate than that observed in a conventional FC- (or normal-state) experiment. This procedure is particularly suited for evaluating the SC volume fraction of superconductors with a weak magnetic-flux expulsion, as the H-doped TiSe$_2$ in the present case.

Muon spin rotation fits. In all cases, the time-dependent TF polarization was fitted using the following function:

$$\begin{aligned} P_{TF}(t) = &f_{sc}\cos(\gamma_\mu B_\mu t + \phi)\exp(-\sigma^2 t^2/2) \\ &+ f_{tail}\cos(\gamma_\mu B_{tail} t + \phi)\exp(-\Lambda t) \end{aligned} \tag{4}$$

Here, $f_{tail} = 1 - f_{sc}$ is the fraction of muons implanted in the silver degrader and in the non SC parts of the sample, $\gamma_\mu/2\pi = 135.53$ MHz/T is the muon gyromagnetic ratio, B_μ and B_{tail} are the magnetic fields probed by the muons implanted in the sample and in the silver degrader, and ϕ is a common initial phase. Finally, Λ is the relaxation rate originating from the muons implanted in the silver degrader.

Both Λ and f_{tail} parameters were obtained in a two-step calibration via a ZFC TF experiment at 0.28 K (see Fig. 4). First, the long-time tail ($t > 5$ μs) was fitted with a single oscillating component ($f_{sc} = 0$), determining $\Lambda = 30 \pm 6$ ns^{-1}. In this case, due to the fast signal decay in the SC phase, the long-time tail reflects only those muons implanted in the silver degrader (and in non-SC parts of the sample). Secondly, by fixing Λ to the previously determined value, the data were fitted over

the whole time range to obtain $f_{tail} = 0.56 \pm 0.02$. These two parameters were then kept fixed during all the subsequent TF-fits.

From the SC depolarization rate σ_{sc}, under the assumption of an ideal triangular vortex lattice, and by considering that the applied field is negligibly small with respect to the upper critical field determined from resistivity and magnetization measurements ($H_{c2} > 0.1$ T), the magnetic penetration depth is determined as $\lambda = (0.00371\Phi_0 \gamma_\mu^2/\sigma_{sc}^2)^{1/4}$[81,82].

Density functional theory calculations. First-principles calculations were performed using the QUANTUM ESPRESSO package[83,84]. For all calculations, the experimental lattice parameters and the Generalized Gradient Approximation (GGA) for the exchange and correlation energy were adopted. This is because in $1T$-$TiSe_2$ the GGA functional, on top of the experimentally determined lattice constants, successfully predicts both the internal structural parameters (Se-Ti distance) and the dynamical instabilities guiding the system to the $2 \times 2 \times 2$ charge density wave phase[85], in perfect agreement with experiments. Conversely, since the GGA functional does not describe perfectly the electronic properties of $TiSe_2$ due to the strong correlation effects arising from the localized d orbitals of Ti[85,86], the effects of local correlations were accounted for by including a Hubbard-like correction for Ti-d orbitals in a GGA+U approach[87]. The U parameter, determined from first principles[85,88], was set to $U = 3.9$ eV, allowing to reproduce the Fermi surface experimentally determined via angle-resolved photoemission spectroscopy[86,89,90]. Electron–ion interaction was described with pseudopotentials that include the $3s$, $3p$, $4s$ and $3d$ valence states for Ti and $4s$, $4p$ and $4d$ for Se, with an energy cutoff up to 70 Ry (840 Ry for charge density). The integration over the Brillouin Zone (BZ) was performed using a uniform $24 \times 24 \times 14$ grid (for the $TiSe_2$ unit cell, and properly rescaled for the supercell calculations) with a 0.005 Ry Gaussian smearing. The electronic density of states are evaluated sampling the BZ on a $30 \times 30 \times 18$ uniform grid using tetrahedron method for integration[91]. Several structural models, starting from low concentration regime up to higher doping, were considered using a random-search algorithm (over 100 configurations) to determine the H atom's lowest-energy intercalation site. One H atom is placed in a $2 \times 2 \times 2$ $1T$-$TiSe_2$ supercell in the lowest concentration ($x = 0.125$), whereas two H atoms are included in the $1 \times 1 \times 1$ unit cell ($x = 2$) in the highest. In the low concentration regime, we unfold the electronic bands onto the $1T$-$TiSe_2$ BZ by means of the Bands-UP software[92,93]. The application of an external pressure of ~10 GPa was realized by reducing the lattice constants of about 4% at constant c/a ratio, where c and a are the out-of-plane and in-plane lattice constants respectively. Phonon calculations were performed using the Density Functional Perturbation Theory[94] in the harmonic approximation sampling the reciprocal space with a $4 \times 4 \times 4$ grid. The electron–phonon coupling was converged using a $48 \times 48 \times 28$ k-point grid for the electronic momenta. The SC critical temperature was estimated using the Allen-Dynes modified Mc-Millan equation[95,96] with $\mu^* = 0.1$[69,97] (see also Supplementary Note 8).

Data availability
The data that support the findings of this study are available from the authors upon reasonable request.

References
1. Drozdov, A. P., Eremets, M. I., Troyan, I. A., Ksenofontov, V. & Shylin, S. I. Conventional superconductivity at 203 kelvin at high pressures in the sulfur hydride system. *Nature* **525**, 73–76 (2015).
2. Drozdov, A. P. et al. Superconductivity at 250 K in lanthanum hydride under high pressures. *Nature* **569**, 528–531 (2019).
3. Dasenbrock-Gammon, N. et al. Evidence of near-ambient superconductivity in a N-doped lutetium hydride. *Nature* **615**, 244–250 (2023).
4. Lu, N. et al. Electric-field control of tri-state phase transformation with a selective dual-ion switch. *Nature* **546**, 124–128 (2017).
5. Jo, M. et al. Gate-induced massive and reversible phase transition of VO_2 channels using solid-state proton electrolytes. *Adv. Funct. Mater.* **28**, 1802003 (2018).
6. Rafique, M. et al. Ionic liquid gating induced protonation of electron-doped cuprate superconductors. *Nano Lett.* **19**, 7775–7780 (2019).
7. Li, Z. et al. Reversible manipulation of the magnetic state in $SrRuO_3$ through electric-field controlled proton evolution. *Nat. Commun.* **11**, 184 (2020).
8. Wang, M. et al. Manipulate the electronic state of Mott iridate superlattice through protonation induced electron-filling. *Adv. Funct. Mater.* **31**, 2100261 (2021).
9. Shen, S. et al. Emergent ferromagnetism with Fermi-liquid behavior in proton intercalated $CaRuO_3$. *Phys. Rev. X* **11**, 021018 (2021).
10. Cui, Y. et al. Ionic-liquid-gating induced protonation and superconductivity in FeSe, $FeSe_{0.93}S_{0.07}$, $ZrNCl$, $1T$-TaS_2 and Bi_2Se_3. *Chin. Phys. Lett.* **36**, 077401 (2019).
11. Meng, Y. et al. Protonation-induced discrete superconducting phases in bulk FeSe single crystals. *Phys. Rev. B* **105**, 134506 (2022).
12. Manzeli, S., Ovchinnikov, D., Pasquier, D., Yazyev, O. V. & Kis, A. 2D transition metal dichalcogenides. *Nat. Rev. Mater.* **2**, 17033 (2017).
13. Choi, W. et al. Recent development of two-dimensional transition metal dichalcogenides and their applications. *Mater. Today* **20**, 116–130 (2017).
14. Fu, L. & Kane, C. L. Superconducting proximity effect and Majorana fermions at the surface of a topological insulator. *Phys. Rev. Lett.* **100**, 096407 (2008).
15. Li, Y. W. et al. Observation of topological superconductivity in a stoichiometric transition metal dichalcogenide $2M$-WS_2. *Nat. Commun.* **12**, 2874 (2021).
16. Wang, Q. H., Kalantar-Zadeh, K., Kis, A., Coleman, J. N. & Strano, M. S. Electronics and optoelectronics of two-dimensional transition metal dichalcogenides. *Nat. Nanotechnol.* **7**, 699–712 (2012).
17. Fiori, G. et al. Electronics based on two-dimensional materials. *Nat. Nanotechnol.* **9**, 768–779 (2014).
18. Zhu, W., Low, T., Wang, H., Ye, P. & Duan, X. Nanoscale electronic devices based on transition metal dichalcogenides. *2D Mater.* **6**, 032004 (2017).
19. Li, J. et al. Printable two-dimensional superconducting monolayers. *Nat. Mater.* **20**, 181–187 (2021).
20. Piatti, E. et al. Charge transport mechanisms in inkjet-printed thin-film transistors based on two-dimensional materials. *Nat. Electron.* **4**, 893–905 (2021).
21. Lian, B., Sun, X.-Q., Vaezi, A., Qi, X.-L. & Zhang, S.-C. Topological quantum computation based on chiral Majorana fermions. *Proc. Natl. Acad. Sci. USA* **115**, 10938–10942 (2018).
22. Stewart, G. R. Superconductivity in iron compounds. *Rev. Mod. Phys.* **83**, 1589 (2011).
23. Fernandes, R. M. et al. Iron pnictides and chalcogenides: a new paradigm for superconductivity. *Nature* **601**, 7891 (2022).
24. Shen, K. M. & Davis, J. S. Cuprate high-T_c superconductors. *Mater. Today* **11**, 14–21 (2008).
25. Stewart, G. R. Heavy-fermion systems. *Rev. Mod. Phys.* **56**, 755 (1984).
26. Morosan, E. et al. Superconductivity in Cu_xTiSe_2. *Nat. Phys.* **2**, 544–550 (2006).
27. Morosan, E. et al. Multiple electronic transitions and superconductivity in Pd_xTiSe_2. *Phys. Rev. B* **81**, 094524 (2010).
28. Sato, K. et al. New lithium- and diamines-intercalated superconductors $Li_x(C_2H_8N_2)_yTiSe_2$ and $Li_x(C_6H_{16}N_2)_yTiSe_2$. *J. Phys. Soc. Jpn.* **86**, 104701 (2017).
29. Kusmartseva, A. F., Sipos, B., Berger, H., Forro, L. & Tutiš, E. Pressure induced superconductivity in pristine $1T$-$TiSe_2$. *Phys. Rev. Lett.* **103**, 236401 (2009).
30. Li, L. J. et al. Controlling many-body states by the electric-field effect in a two-dimensional material. *Nature* **529**, 185–189 (2016).
31. Li, L. et al. Anomalous quantum metal in a 2D crystalline superconductor with electronic phase nonuniformity. *Nano Lett.* **19**, 4126–4133 (2019).
32. Boeri, L. et al. The 2021 room-temperature superconductivity roadmap. *J. Phys.: Condens. Matter* **34**, 183002 (2022).
33. Liao, M. et al. Coexistence of resistance oscillations and the anomalous metal phase in a lithium intercalated $TiSe_2$ superconductor. *Nat. Commun.* **12**, 5342 (2021).
34. Wu, G. et al. Transport properties of single-crystalline Cu_xTiSe_2 ($0.015 \leq x \leq 0.110$). *Phys. Rev. B* **76**, 024513 (2007).
35. Wang, Y., Nakano, M., Kashiwabara, Y., Matsuoka, H. & Iwasa, Y. Transport properties of a few nanometer-thick $TiSe_2$ films grown by molecular-beam epitaxy. *Appl. Phys. Lett.* **113**, 073101 (2018).
36. Di Salvo, F. J., Moncton, D. E. & Waszczak, J. V. Electronic properties and superlattice formation in the semimetal $TiSe_2$. *Phys. Rev. B* **14**, 4321 (1976).
37. Jaouen, T. et al. Phase separation in the vicinity of Fermi surface hot spots. *Phys. Rev. B* **100**, 075152 (2019).
38. Huang, S. H., Shu, G. J., Pai, W. W., Liu, H. L. & Chou, F. C. Tunable Se vacancy defects and the unconventional charge density wave in $1T$-$TiSe_{2-\delta}$. *Phys. Rev. B* **95**, 045310 (2017).
39. Campbell, D. J. et al. Intrinsic insulating ground state in transition metal dichalcogenide $TiSe_2$. *Phys. Rev. Mater.* **3**, 053402 (2019).
40. Watson, M. D., Beales, A. M. & King, P. D. C. On the origin of the anomalous peak in the resistivity of $TiSe_2$. *Phys. Rev. B* **99**, 195142 (2019).
41. Li, L. J. et al. Enhancing charge-density-wave order in $1T$-$TiSe_2$ nanosheet by encapsulation with hexagonal boron nitride. *Appl. Phys. Lett.* **109**, 141902 (2016).
42. Duong, D. L. et al. Raman characterization of the charge density wave phase of $1T$-$TiSe_2$: from bulk to atomically thin layers. *ACS Nano* **11**, 1034–1040 (2017).

43. Holy, J. A., Woo, K. C., Klein, M. V. & Brown, F. C. Raman and infrared studies of superlattice formation in TiSe$_2$. *Phys. Rev. B* **16**, 3628 (1977).

44. Sugai, S., Murase, K., Uchida, S. & Tanaka, S. Raman studies of lattice dynamics in 1*T*-TiSe$_2$. *Solid State Commun.* **35**, 433–436 (1980).

45. Uchida, S. & Sugai, S. Infrared and Raman studies on commensurate CDW states in transition metal dichalcogenides. *Phys. B+C* **105**, 393–399 (1981).

46. Jaswal, S. S. Lattice dynamics of TiSe$_2$. *Phys. Rev. B* **20**, 5297 (1979).

47. Futera, Z. et al. Vibrational modes of hydrogen hydrates: a first-principles molecular dynamics and Raman spectra study. *J. Phys. Chem. C* **121**, 3690–3696 (2017).

48. Okamoto, Y., Saito, M. & Oshiyama, A. Comparative study of vibrational frequencies of H$_2$ molecules in Si and GaAs. *Phys. Rev. B* **56**, R10016 (1997).

49. Zhao, J. F. et al. Evolution of the electronic structure of 1*T*-Cu$_x$TiSe$_2$. *Phys. Rev. Lett.* **99**, 146401 (2007).

50. Spera, M., Scarfato, A., Giannini, E. & Renner, C. Energy-dependent spatial texturing of charge order in 1*T*-Cu$_x$TiSe$_2$. *Phys. Rev. B* **99**, 155133 (2019).

51. Spera, M. et al. Insight into the charge density wave gap from contrast inversion in topographic STM images. *Phys. Rev. Lett.* **125**, 267603 (2020).

52. Cho, K. et al. Using controlled disorder to probe the interplay between charge order and superconductivity in NbSe$_2$. *Nat. Commun.* **9**, 2796 (2018).

53. Knowles, P. et al. Fermi surface reconstruction and electron dynamics at the charge-density-wave transition in TiSe$_2$. *Phys. Rev. Lett.* **124**, 167602 (2020).

54. Slichter, C. P. *Principles of magnetic resonance* 3 edn, (Springer-Verlag, Berlin, Heidelberg, 1990).

55. Tsuda, T., Kitaoka, Y. & Yasuoka, H. NMR studies of the CDW state in 1T-VSe$_2$. *Phys. B+C* **105**, 414 (1981).

56. Tsuda, T., Yasuoka, H., Kitaoka, Y. & Di Salvo, F. J. ^{51}V NMR study of the phase transition in 1T-VS$_2$. *J. Magn. Magn. Mater.* **31-34**, 1101 (1983).

57. Mizuno, K. et al. ^{125}Te NMR study of IrTe$_2$. *Phys. B: Condens. Matter* **312-313**, 818 (2002).

58. Prando, G., Piatti, E., Daghero, D., Gonnelli, R. S. & Carretta, P. Cluster charge-density-wave glass in hydrogen-intercalated TiSe$_2$. Preprint at https://doi.org/10.48550/arXiv.2307.10979 (2023).

59. Dupree, R., Warren, W. W. J. & Di Salvo, F. J. J. ^{77}Se NMR study of the electronic instability in TiSe$_2$. *Phys. Rev. B* **16**, 1001 (1977).

60. Blatter, G., Feigel'man, M. V., Geshkenbein, V. B., Larkin, A. I. & Vinokur, V. M. Vortices in high-temperature superconductors. *Rev. Mod. Phys.* **66**, 1125 (1994).

61. Xing, X. et al. Two-band and Pauli-limiting effects on the upper critical field of 112-type iron pnictide superconductors. *Sci. Rep.* **7**, 45943 (2017).

62. Gurevich, A. Enhancement of the upper critical field by nonmagnetic impurities in dirty two-gap superconductors. *Phys. Rev. B* **67**, 184515 (2003).

63. Ding, D. et al. Multivalley superconductivity in monolayer transition metal dichalcogenides. *Nano Lett.* **22**, 7919–7926 (2022).

64. Blundell, S. J. Spin-polarized muons in condensed matter physics. *Contemp. Phys.* **40**, 175–192 (1999).

65. Amato, A. Heavy-fermion systems studied by μSR technique. *Rev. Mod. Phys.* **69**, 1119–1180 (1997).

66. Tresca, C. & Calandra, M. Charge density wave and spin 1/2 insulating state in single layer 1*T*-NbS$_2$. *2D Mater.* **6**, 035041 (2019).

67. Noat, Y. et al. Quasiparticle spectra of 2*H*-NbSe$_2$: two-band superconductivity and the role of tunneling selectivity. *Phys. Rev. B* **92**, 134510 (2015).

68. Heil, C. et al. Origin of superconductivity and latent charge density wave in NbS$_2$. *Phys. Rev. Lett.* **119**, 087003 (2017).

69. Calandra, M. & Mauri, F. Charge-density wave and superconducting dome in TiSe$_2$ from electron-phonon interaction. *Phys. Rev. Lett.* **106**, 196406 (2011).

70. Vocaturo, R., Tresca, C., Ghiringhelli, G. & Profeta, G. Prediction of ambient-pressure superconductivity in ternary hydride PdCuH$_x$. *J. Appl. Phys.* **131**, 033903 (2022).

71. Flores-Livas, J. A. et al. A perspective on conventional high-temperature superconductors at high pressure: methods and materials. *Phys. Rep.* **856**, 1–78 (2020).

72. Bekaert, J., Petrov, M., Aperis, A., Oppeneer, P. M. & Milošević, M. V. Hydrogen-induced high-temperature superconductivity in two-dimensional materials: the example of hydrogenated monolayer MgB$_2$. *Phys. Rev. Lett.* **123**, 077001 (2019).

73. Wang, H. et al. Hydrogenation as a source of superconductivity in two-dimensional TiB$_2$. *Int. J.Mod. Phys. C* **32**, 2150057 (2021).

74. Yu, S. et al. Pressure-driven formation and stabilization of superconductive chromium hydrides. *Sci. Rep.* **5**, 17764 (2015).

75. Jiao, N. et al. Hydrogenation induced high-temperature superconductivity in two-dimensional molybdenum carbide Mo$_2$C$_3$. *Europhys. Lett.* **138**, 46002 (2022).

76. Rawal, T. B., Chang, L.-H., Liu, H.-D., Lu, H.-Y. & Ting, C. S. Phonon-mediated superconductivity near the lattice instability in hole-doped hydrogenated monolayer hexagonal boron nitride. *Phys. Rev. Mater.* **6**, 054003 (2022).

77. Sanna, A., Davydov, A., Dewhurst, J. K., Sharma, S. & Flores-Livas, J. A. Superconductivity in hydrogenated carbon nanostructures. *Eur. Phys. J. B* **91**, 177 (2018).

78. Shiogai, J., Ito, Y., Mitsuhashi, T., Nojima, T. & Tsukazaki, A. Electric-field-induced superconductivity in electrochemically etched ultrathin FeSe films on SrTiO$_3$ and MgO. *Nat. Phys.* **12**, 42–46 (2016).

79. Piatti, E., Montagna Bozzone, J. & Daghero, D. Anomalous metallic phase in molybdenum disulphide induced via gate-driven organic ion intercalation. *Nanomaterials* **12**, 1842 (2022).

80. O'Neill, B., Nguyen, J. H. & Jealoz, R. Rapid computer analysis of X-ray diffraction films. *Am. Miner.* **78**, 1332–1335 (1993).

81. Barford, W. & Gunn, J. M. F. The theory of the measurement of the London penetration depth in uniaxial type II superconductors by muon spin rotation. *Phys. C* **156**, 515–522 (1988).

82. Brandt, E. H. Properties of the ideal Ginzburg-Landau vortex lattice. *Phys. Rev. B* **68**, 054506 (2003).

83. Giannozzi, P. et al. QUANTUM ESPRESSO: a modular and open-source software project for quantum simulations of materials. *J. Phys. Condens. Matter* **21**, 395502 (2009).

84. Giannozzi, P. et al. Advanced capabilities for materials modelling with QUANTUM ESPRESSO. *J. Phys. Condens. Matter* **29**, 465901 (2017).

85. Bianco, R., Calandra, M. & Mauri, F. Electronic and vibrational properties of TiSe$_2$ in the charge-density-wave phase from first principles. *Phys. Rev. B* **92**, 094107 (2015).

86. Rohwer, T. et al. Collapse of long-range charge order tracked by time-resolved photoemission at high momenta. *Nature* **471**, 490–493 (2011).

87. Anisimov, V. I., Zaanen, J. & Andersen, O. K. Band theory and Mott insulators: Hubbard U instead of Stoner I. *Phys. Rev. B* **44**, 943–954 (1991).

88. Cococcioni, M. & De Gironcoli, S. Linear response approach to the calculation of the effective interaction parameters in the LDA+U method. *Phys. Rev. B* **71**, 035105 (2005).

89. Rasch, J. C. E., Stemmler, T., Müller, B., Dudy, L. & Manzke, R. 1*T*-TiSe$_2$: semimetal or semiconductor? *Phys. Rev. Lett.* **101**, 237602 (2008).

90. Watson, M. D. et al. Orbital-and k$_z$-selective hybridization of Se 4*p* and Ti 3*d* states in the charge density wave phase of TiSe$_2$. *Phys. Rev. Lett.* **122**, 076404 (2019).

91. Kawamura, M., Gohda, Y. & Tsuneyuki, S. Improved tetrahedron method for the brillouin-zone integration applicable to response functions. *Phys. Rev. B* **89**, 094515 (2014).

92. Medeiros, P. V. C., Stafström, S. & Björk, J. Effects of extrinsic and intrinsic perturbations on the electronic structure of graphene: retaining an effective primitive cell band structure by band unfolding. *Phys. Rev. B* **89**, 041407 (2014).

93. Medeiros, P. V. C., Tsirkin, S. S., Stafström, S. & Björk, J. Unfolding spinor wave functions and expectation values of general operators: introducing the unfolding-density operator. *Phys. Rev. B* **91**, 041116 (2015).

94. Gonze, X. Perturbation expansion of variational principles at arbitrary order. *Phys. Rev. A* **52**, 1086 (1995).

95. Dynes, R. McMillan's equation and the T$_c$ of superconductors. *Solid State Commun.* **10**, 615–618 (1972).

96. Allen, P. B. & Dynes, R. C. Transition temperature of strong-coupled superconductors reanalyzed. *Phys. Rev. B* **12**, 905–922 (1975).

97. Wei, M. J. et al. Manipulating charge density wave order in monolayer 1*T* − TiSe$_2$ by strain and charge doping: a first-principles investigation. *Phys. Rev. B* **96**, 165404 (2017).

Acknowledgements

Author contributions

E.P., G.P. and R.S.G. conceived the idea. R.S.G. directed the project. E.P., D.D., and R.S.G. designed and performed the protonation and the electric transport measurements. G.P. and P.C. performed the NMR characterization. M.M. and M.P. contributed to the electric transport measurements. C.T. and G.P. performed the ab initio calculations. S.R. provided the pristine samples and performed the XRD characterization. G.L. performed the magnetization measurements. G.P., G.L., and T.S. performed the μSR measurements. All authors contributed to the discussion and interpretation of the results. E.P., G.P., G.L., T.S., G.P., D.D. and R.S.G. wrote the manuscript with input from all authors.

Competing interests

The authors declare no competing interests.

Additional information

Correspondence and requests for materials should be addressed to Erik Piatti or Renato S. Gonnelli.

Reprints and permission information is available at http://www.nature.com/reprints

Publisher's note Springer Nature remains neutral with regard to jurisdictional claims in published maps and institutional affiliations.